



# A Cloud-Ozone Data Product from Aura OMI and MLS Satellite Measurements

Jerald R. Ziemke<sup>1,2</sup>, Sarah A. Strode<sup>2,3</sup>, Anne R. Douglass<sup>2</sup>, Joanna Joiner<sup>2</sup>, Alexander Vasilkov<sup>2,4</sup>, Luke D. Oman<sup>2</sup>, Junhua Liu<sup>2,3</sup>, Susan E. Strahan<sup>2,3</sup>, Pawan K. Bhartia<sup>2</sup>, David P. Haffner<sup>2,4</sup>

<sup>1</sup>Morgan State University, Baltimore, Maryland, USA

<sup>2</sup>NASA Goddard Space Flight Center, Greenbelt, Maryland, USA

<sup>3</sup>Universities Space Research Association, Columbia, MD, USA

<sup>4</sup>SSAI, Lanham, Maryland, USA

**Abstract.** Ozone within deep convective clouds is controlled by several factors involving photochemical reactions and transport. Gas-phase photochemical reactions, and heterogeneous surface chemical reactions involving ice, water particles, and aerosols inside the clouds all contribute to the distribution and net production and loss of ozone. Ozone in clouds is also dependent on convective transport that carries low troposphere/boundary layer ozone and ozone precursors upward into the clouds. Characterizing ozone in thick clouds is an important step for quantifying relationships of ozone with tropospheric H<sub>2</sub>O, OH production, and cloud microphysics/transport properties. Although measuring ozone in deep convective clouds from either aircraft or balloon ozonesondes is largely impossible due to extreme meteorological conditions associated with these clouds, it is possible to estimate ozone in thick clouds using backscattered solar UV radiation measured by satellite instruments. Our study combines Aura Ozone Monitoring Instrument (OMI) and Microwave Limb Sounder (MLS) satellite measurements to generate a new research product, monthly-mean ozone concentrations in deep convective clouds between 30°S to 30°N for October 2004 – April 2016. These measurements reveal key features of cloud ozone including: persistent low ozone concentrations in the tropical



Pacific of ~10 ppbv or less; concentrations of up to 60 ppbv or greater over landmass regions of South America, southern Africa, Australia, and India/east Asia; connections with tropical ENSO events; and intra-seasonal/Madden-Julian Oscillation variability. Analysis of OMI aerosol measurements suggests a cause and effect relation between boundary layer pollution and elevated ozone inside thick clouds over land-mass regions including southern Africa and India/east Asia.

36

## 1. Introduction.

38

Measuring tropospheric ozone in deep convective clouds including convective outflow regions in the mid-upper troposphere is important for several reasons. Ozone in the upper troposphere is a major greenhouse gas that contributes to climate forcing. The IPCC 2013 Report (e.g., in Hartmann et al., 2014; <http://www.ipcc.ch/report/ar5/wg1/>) includes an evaluation of tropospheric versus stratospheric ozone using a collage of radiative transfer model calculations. The report shows that the radiative forcing of tropospheric ozone is 10 times greater than that of stratospheric ozone, even though only 10% of the atmospheric ozone resides in the troposphere. The IPCC 2013 report (and references therein) also notes that ozone is a major surface pollutant, and is important as the main source of OH, the primary cleanser of pollutants in the troposphere. Measurements of ozone associated with deep convection are needed to characterize the extent of ozone inter-relationships with tropospheric H<sub>2</sub>O and OH production, and in understanding cloud microphysics/transport properties and resulting influence on global and regional tropospheric ozone distributions.

52

Microphysics and photochemistry can be very complex for deep convective clouds. Huntrieser et al. (2016, and references therein) combined aircraft and cloud measurements with a model to study ozone distributions and sources associated with deep convective clouds over the central U.S. Huntrieser et al. (2016) identified upward transport of lower tropospheric ozone and ozone precursors into the upper troposphere within thick clouds. They also showed that cloud tops over-shoot the tropopause and inject high amounts of biomass burning pollutants (largely CO and NO<sub>x</sub>) and lightning-produced NO<sub>x</sub> into the low stratosphere, while at the same time ozone-rich air from the low stratosphere is transported downward into the cloud anvil and surrounding



61 outflow regions as a dynamical response to overshooting. Some of the Geostationary  
62 Operational Environmental Satellite (GOES) cloud tops were found to reach up to 17-18 km  
63 altitude for these deep convective systems. Pronounced ozone-rich stratospheric air was  
64 observed within cloud outflow regions.

65

66 The ozonesonde measurement record includes occurrences of very low to even “near-zero”  
67 ozone concentrations in the tropical upper troposphere associated with the passing of deep  
68 convective cloud systems (e.g., Kley et al., 1996; Folkins et al., 2002; Solomon et al., 2005).  
69 The very low ozone values are largely attributed to convective lifting of low concentrations of  
70 ozone from the marine boundary layer into the upper troposphere. In pollution-free oceanic  
71 regions it is not uncommon for ozone in the marine boundary layer to be only a few ppbv due to  
72 ozone net loss reactions involving hydrogen radicals OH and HO<sub>2</sub> (e.g., Solomon et al., 2005,  
73 and references therein). Some studies suggest the possibility of in-cloud photochemical ozone  
74 destruction mechanisms (e.g., Zhu et al., 2001; Barth et al., 2002; Liu et al., 2006). Vömel and  
75 Diaz (2010) showed that improperly calibrated Electrochemical Concentration Cell (ECC)  
76 ozonesondes led to a small measurement error (under-determination) and the near-zero upper  
77 troposphere ozone concentrations reported in these studies. Vömel and Diaz (2010) found that  
78 the near-zero ozone concentrations in the upper troposphere were instead about 10 ppbv and  
79 attributed the calibration error to unaccounted variations associated with background cell  
80 currents at launch. Vömel and Diaz (2010) indicate that the studies measuring “near-zero” ozone  
81 were not wrong, but instead slightly underdetermined the low ozone concentrations.

82

83 The very low ozone measurements in the tropical upper troposphere in past studies were  
84 obtained from a limited number of aircraft flights and ozonesondes at a few isolated sites in the  
85 vicinity of, but not inside, deep convective cloud systems. Measuring ozone directly inside deep  
86 convective clouds from ozonesondes and aircraft instruments remains an elusive task due to  
87 extreme meteorological conditions associated with the clouds. Ziemke et al. (2009) developed a  
88 residual “cloud slicing” method for measuring ozone volume mixing ratios within thick clouds  
89 by combining Aura Ozone Monitoring Instrument (OMI) and Microwave Limb Sounder (MLS)  
90 satellite measurements. For deep convective clouds, OMI provided the tropospheric cloud ozone  
91 measurements after subtracting co-located MLS stratospheric column ozone. Their study found



large variability in the ozone concentrations in thick clouds. While very low ozone concentrations ( $< 10$  ppbv) in the clouds were identified in the remote Indian and Pacific Ocean regions, concentrations greater than 60 ppbv were obtained over continental landmasses including Africa. Ziemke et al. (2009) hypothesized that the ozone measured in thick clouds is largely a manifestation of ozone concentrations (from low to high amounts) present in the low troposphere/boundary layer that become transported upward by convection.

We build upon the cloud slicing work of Ziemke et al. (2009) to produce a long data record of OMI/MLS cloud ozone measurements as that former study was limited to only a few months of measurements from years 2005 and 2006. As with Ziemke et al. (2009), we derive ozone mixing ratios inside tropical deep convective clouds by combining Aura OMI measurements of total column ozone and cloud pressure with Aura MLS stratospheric column ozone. This paper is organized as follows: Section 2 details the satellite measurements while Section 3 is an overview of cloud slicing. Section 4 discusses validation and Sections 5-6 discuss basic characteristics and scientific interpretations of the data. Finally, Section 7 provides a summary.

## 2. Satellite Measurements.

Our study combines Aura OMI and MLS ozone measurements with OMI aerosols and cloud parameters (i.e., cloud pressures, radiative cloud fractions). OMI is a UV/VIS solar backscatter spectrometer that makes daily measurements of Earth radiances and solar irradiances from 270 to 500 nm with spectral resolution of about 0.5 nm (Levelt et al., 2006). OMI scans perpendicular to the orbit path with 60 side-scan positions and provides near-global coverage of the sunlit Earth with a pixel size of  $13 \text{ km} \times 24 \text{ km}$  at nadir. Description and access to the OMI v8.5 data can be obtained from the website <http://disc.sci.gsfc.nasa.gov/Aura/data-holdings/OMI>. In January 2009 a physical external optical blockage known as the “row anomaly” reduced the number of the 60 good side-scanning row measurements to about 30-40. Scan positions 21-55 are the most affected, with dependence on latitude and specific day. All of the OMI measurements that we use were properly screened to exclude all data affected by the row anomaly artifact.



122 OMI cloud pressures and radiative cloud fractions are derived using UV-2 radiances (Vasilkov et  
123 al., 2008). The cloud pressure from OMI is named optical centroid pressure (OCP). As shown  
124 by Vasilkov et al. (2008), the OCP at UV wavelengths lies deep inside the clouds, often by  
125 several hundred hPa and therefore is not a measure of true cloud top; they showed this by  
126 comparing the OMI OCP measurements with both Cloudsat radar reflectivity profiles and  
127 MODIS IR cloud pressures. The OCP effectively represents the bottom reflecting surface for the  
128 OMI retrievals in the presence of clouds. The true ozone measurement from OMI is the column  
129 amount from the top of the atmosphere down to the reflecting surface. In the presence of a  
130 cloud, the OMI algorithm places an ozone “ghost column” climatology estimate below the OCP  
131 reflecting surface to obtain total column ozone.

132

133 There are two OMI algorithms that determine the OCP. The first algorithm is based on O<sub>2</sub>-O<sub>2</sub>  
134 dimer absorption (Sneep et al., 2008) and the second is based on rotational-Raman scattering  
135 (RRS) that uses spectral structures in the ratio of backscattered radiance to solar irradiance,  
136 known as the Ring effect (Joiner and Bhartia, 1995; Joiner et al., 2004; Joiner and Vasilkov,  
137 2006). The two OMI cloud algorithms provide similar estimates of OCP for bright clouds  
138 although there are small differences due to algorithmic and physical effects (Sneep et al., 2008).  
139 We use the RRS cloud pressure for our study although our results would be nearly identical  
140 using the O<sub>2</sub>-O<sub>2</sub> cloud measurements. We refer to “cloud ozone” as the ozone column or ozone  
141 mean volume mixing ratio lying between the tropopause and retrieved OCP from OMI under  
142 conditions of deep convection. Deep convective clouds often have cloud tops at or near the  
143 tropopause. Therefore much if not most of the tropospheric ozone measured between the  
144 tropopause and OMI cloud pressure lie within the cloud itself rather than above the cloud top.

145

146 Aura MLS v4.2 profile ozone is included to measure fields of stratospheric column ozone (SCO).  
147 MLS SCO is used in conjunction with OMI above-cloud column ozone each day to derive mean  
148 column amounts and mean concentrations of ozone measured over deep convective clouds. The  
149 MLS ozone profiles are vertically integrated in log-pressure from 0.0215 hPa down to the  
150 tropopause to derive measurements of SCO as described by Ziemke et al. (2006, 2009). To  
151 separate stratospheric from tropospheric ozone we similarly use the WMO 2K-km<sup>-1</sup> lapse-rate  
152 tropopause pressure definition with NCEP re-analysis temperatures. Other tropopause pressure



153 definitions and other meteorological analyses besides NCEP could have also been used. We  
 154 included the WMO definition with NCEP for both historical reasons and consistency checking  
 155 relative to previous versions of our OMI/MLS tropospheric ozone products that used the same  
 156 NCEP tropopause. For the low latitudes in our study we expect that there would be only minor  
 157 differences in our results if we used instead a different tropopause. All MLS v4.2 retrieval  
 158 quality flags (quality, status, convergence, and precision) are properly adhered to for all of our  
 159 analyses. The MLS v4.2 measurements including data quality and quality flags are described in  
 160 the MLS data quality document [http://mls.jpl.nasa.gov/data/v4-2\\_data\\_quality\\_document.pdf](http://mls.jpl.nasa.gov/data/v4-2_data_quality_document.pdf).  
 161 Recommended pressure levels for science applications with MLS v4.2 ozone are 0.0215 hPa to  
 162 261 hPa. With SCO representing column ozone from the top of the atmosphere down to the  
 163 tropopause, all tropospheric ozone measurements in our analyses are independent of any  
 164 stratospheric ozone barring possible unresolved stratospheric intrusions and unknown errors.

165

### 166 **3. Overview of Cloud Slicing.**

167

168 We use two cloud slicing methods to measure cloud ozone from Aura OMI and MLS  
 169 instruments. The first method is called “ensemble” cloud slicing. This algorithm was first  
 170 proposed by Ziemke et al. (2001) and combined co-located Nimbus-7 TOMS column ozone and  
 171 THIR IR cloud-top pressure. Here we combine OMI column ozone with OMI cloud pressure  
 172 (i.e., OCP). An advantage of ensemble cloud ozone is that it requires only a single instrument,  
 173 but weaknesses are noisiness and poor spatial resolution in the measurements. The second  
 174 method is a residual cloud slicing approach (Ziemke et al., 2009) that combines OCPs from OMI  
 175 with residual column ozone differences between OMI and MLS. An advantage of the residual  
 176 method is that it can yield measurements with high horizontal resolution. The cloud ozone  
 177 product that we generate comes from the OMI/MLS residual method. We use OMI ensemble  
 178 measurements only as a consistency check for the OMI/MLS residual ozone.

179

180 A schematic diagram for the ensemble cloud slicing method is shown in Figure 1. A region is  
 181 first chosen (top of figure,  $5^\circ \times 5^\circ$  region shown) with all coincident measurements of above-  
 182 cloud column ozone plotted versus OCP effective cloud pressure (bottom of figure). The OCP as  
 183 noted in Section 2 may lie several hundred hPa below the cloud top, and the OMI algorithm



184 places a climatological ozone ghost column below the OCP to determine total column ozone.  
 185 For cloud slicing we use only the above-cloud ozone from OMI which is the true measurement.  
 186 In practice, we determine the above-cloud column ozone by subtracting the ghost column ozone  
 187 from total column ozone reported in the OMI level-2 orbital datasets.

188

189 In Figure 1 the OMI footprint scene depicted is 100% cloud filled so that the OCP deep inside  
 190 the cloud represents the bottom reflecting surface for the OMI retrieval. In the more general  
 191 case, footprint scenes from OMI will not be 100% cloud filled and we account for this. What we  
 192 actually use for cloud slicing in the Figure 1 schematic is an effective scene pressure ( $P_{EFF}$ ) in  
 193 place of the OCP.  $P_{EFF}$  is derived from  $P_{EFF} = P_{CLOUD} \cdot f + P_{SURFACE} \cdot (1 - f)$ , where  $P_{CLOUD}$  is  
 194 the cloud OCP,  $P_{SURFACE}$  is the Earth surface scene pressure, and  $f$  is the OMI scene radiative  
 195 cloud fraction (Joiner et al., 2009). We use OMI measurements for cloud slicing only when  
 196 radiative cloud fraction  $f$  is greater than 0.80. When  $f$  is equal to 1.0 the calculated  $P_{EFF}$  is  
 197 equivalent to OCP. In our case for deep convective cumulonimbus clouds the cloud tops are  
 198 near tropopause level and so the derived mixing ratio is primarily an average measurement of  
 199 ozone inside the clouds.

200

201 Tropospheric ozone mean volume mixing ratio (VMR) is estimated by fitting a straight line to  
 202 the data pairs of above-cloud column ozone versus OCP over the selected geographical region.  
 203 This method was first described by Ziemke et al. (2001) and is summarized here. Column ozone  
 204 ( $\Delta\Omega$ ) between two altitudes  $z_1$  and  $z_2$  is by definition the number of molecules per unit

205 horizontal area and is calculated by integrating ozone number density  $n$  as  $\Delta\Omega = \int_{z_1}^{z_2} n \cdot dz$ . Using

206 hydrostatic balance  $\partial P / \partial z = -\rho g$  ( $\rho$  is mass density,  $g$  is acceleration of gravity) and assuming  
 207 an invariant acceleration of gravity for the troposphere this expression can be converted to:  $\Delta\Omega$

208 (in Dobson Units, DU;  $1 \text{ DU} = 2.69 \times 10^{20} \text{ molecules-m}^{-2}$ ) =  $C \cdot \int_{P_1}^{P_2} X \cdot dP = C \cdot \bar{X} \cdot (P_2 - P_1)$ ,

209 where  $C = 0.00079 \text{ DU-hPa}^{-1}\text{-ppbv}^{-1}$  and  $\bar{X}$  is ozone mean VMR in units ppbv. It follows that  
 210 ozone mean VMR in the troposphere is  $\bar{X} \text{ (ppbv)} = 1270 \cdot \Delta\Omega / \Delta P$ , or in other words 1270  
 211 multiplied by the slope of the ensemble line fit. The  $2\sigma$  uncertainty for VMR in ppbv is  
 212 determined by multiplying the calculated  $2\sigma$  uncertainty of the slope by 1270. An estimate for





SCO can also be obtained by extrapolating the line fit to the mean tropopause pressure over the region. The above-cloud ozone at the extrapolated tropopause pressure, a direct estimate of SCO, can be compared with MLS SCO to assess how well the ensemble method separates stratospheric from tropospheric column ozone.

An example of ensemble scatter plots is shown in Figure 2 for October 5, 2008. The left scatter plot coincides with the region of southern Africa while the right scatter plot coincides with the western Pacific. Measured ozone mixing ratio is 72 ppbv over southern Africa and 10 ppbv over the western Pacific. The enhanced ozone over southern Africa suggests that ozone produced from regional pollution including biomass burning, which is largest around September-October each year in the SH, reaches the upper regions of the clouds. However, the regional elevated ozone over southern Africa may be caused by other sources including lightning  $\text{NO}_x$ , and transport by the Walker circulation, and mixing of stratospheric air that is transported into the troposphere in response to cloud tops overshooting the tropopause (e.g., Huntrieser et al., 2016, and references therein). The low ozone VMR in the western Pacific in Figure 2 is consistent with low values measured in the vicinity of tropical deep convection by ozonesondes (e.g., Kley et al., 1996; Folkins et al., 2002; Solomon et al., 2005; Vömel and Diaz, 2010).

Figure 3 illustrates the residual technique for measuring cloud ozone. This method combines OMI above-cloud column ozone and OMI OCP with MLS SCO. For a deep convective cloud the OCP lies well inside the cloud with a cloud top often at or near the tropopause, so that much or most of measured tropospheric ozone lies inside the cloud rather than above the cloud top. The relationship (Joiner et al., 2009) to derive residual cloud ozone VMR (units ppbv) is  $\text{VMR} = 1270 \cdot [\Delta\Omega / (P_{\text{EFF}} - P_{\text{TROPOPAUSE}})]$ , where  $\Delta\Omega$  is the difference (in DU) of OMI above-cloud column ozone minus MLS SCO,  $P_{\text{TROPOPAUSE}}$  is tropopause pressure (in hPa), and  $P_{\text{EFF}}$  is the effective scene pressure (also in hPa) as defined above. The number 1270 is the same as for the ensemble method to ensure units ppbv for VMR.

#### 4. OMI/MLS Residual Cloud Ozone Product: Validation and Consistency Checks.





243 The validation of OMI/MLS residual cloud ozone measurements is not straightforward given the  
244 paucity of in-cloud measurements from independent sources such as ozonesondes and aircraft.  
245 However, as one approach similar to Ziemke et al. (2009), we can still obtain at least a  
246 consistency check between the OMI/MLS residual cloud ozone and cloud ozone obtained from  
247 the OMI-only ensemble method.

248

249 Figure 4 compares cloud ozone from the ensemble and residual techniques for July 2015 (left  
250 panels) and October 2015 (right panels). Both of these months coincide with the intense 2014-  
251 2016 El Nino. The panels in Figure 4 compare OMI/MLS residual cloud ozone (thick curves)  
252 and OMI ensemble cloud ozone (asterisks). The 5°S-10°N latitude band was chosen because it  
253 includes much of the ITCZ with thick clouds for these months. Both the ensemble and residual  
254 cloud ozone in Figure 4 are low to near zero in the eastern and western Pacific close to the  
255 dateline; it is conceivable that these oceanic regions coincide generally with pristine air and low  
256 concentrations of both ozone and ozone precursors in the boundary layer. In contrast, over a  
257 broad region extending from the western Pacific to Indonesia the cloud ozone from both  
258 measurements is enhanced. The increased tropospheric ozone is due to a combination of  
259 suppressed convection during El Nino and increases in biomass burning over Sumatra and  
260 Borneo due to the induced dry conditions and wildfires (e.g., Chandra et al., 1998; Logan et al.,  
261 2008). The suppressed convection during El Nino coincides with reduced upward injection of  
262 low ozone concentrations in the oceanic boundary layer compared to non-El Nino years, thus  
263 contributing to anomalous increase in cloud ozone relative to non-ENSO years. In the central  
264 Atlantic the cloud ozone measurements are ~50 ppbv for both methods indicating higher ozone  
265 concentrations injected into the clouds from below and in general a more polluted region  
266 compared to the Pacific. In the eastern Atlantic extending to the Indian Ocean / western Pacific  
267 (i.e., ~60°–120°) the ensemble measurements are larger than for OMI/MLS. The calculated  $\pm 2\sigma$   
268 uncertainties for the ensemble measurements are large everywhere including this broad region  
269 and illustrate the noisy nature of the ensemble method. Unlike measurements for the OMI/MLS  
270 residual method, large errors in ozone for the ensemble method may originate largely from the  
271 basic assumptions of the methodology such as uniformity of both SCO and tropospheric mixing  
272 ratio throughout the chosen region. In the next two sections we discuss the OMI/MLS cloud  
273 ozone product for basic geophysical characteristics including some science results.



274

275

## 276 **5. Monthly Distributions.**

277

278 Figure 5 shows monthly-mean climatology maps of OMI/MLS residual cloud ozone derived  
 279 from averaging similar months over the long record. Plotted in Figure 5 is mean VMR (units  
 280 ppbv) representing average ozone concentration lying between the tropopause and OMI OCP as  
 281 described in Section 3. In Figure 5 the mean mixing ratio is calculated for OCPs varying  
 282 between 250 hPa and 550 hPa. The black regions in the figure indicate not enough deep  
 283 convective clouds present and/or mostly clouds such as low-marine stratus clouds with OCP  
 284 lying below the 550 hPa threshold.

285

286 The distributions in Figure 5 illustrate the large regional and temporal variability present in  
 287 cloud-ozone. In the remote Pacific and Indian Ocean regions the values of cloud ozone are small  
 288 at ~10 ppbv or less. High values reaching 70-80 ppbv are measured for landmass regions of  
 289 India/east Asia, southern Africa and South America, and Australia. The high ozone is indicative  
 290 of a more polluted lower troposphere/boundary layer.

291

292 Figure 6 shows climatology maps similar to Figure 5 but instead for “background” ozone mean  
 293 VMR. The east-west tropical wave-1 pattern in tropospheric ozone (Fishman et al., 1990) is  
 294 easily discerned year round in Figure 6 with high values ~60-80 ppbv in the Atlantic and low  
 295 values ~20 ppbv in the eastern and western Pacific. According to Sauvage et al. (2007) using the  
 296 GEOS-Chem Chemical Transport Model (CTM) the main source of tropospheric ozone in the  
 297 tropical Atlantic on annual-mean basis comes from lightning  $\text{NO}_x$  with smaller contributions  
 298 from biomass burning, soils, and fossil fuels (by factors varying ~4-6). Their CTM also  
 299 indicated that stratosphere-troposphere exchange (STE) accounts for less than about 5% of ozone  
 300 in the tropical Atlantic and that most of the effects from  $\text{NO}_x$  came from Africa. In the SH  
 301 subtropics in Figure 6 there is a buildup of high ozone in August-November along all longitudes.  
 302 Although the SH Atlantic maximum in Figure 6 occurs in every month year round, this feature  
 303 also exhibits substantial inter-annual variability. Liu et al. (2017) combined GEOS-5 assimilated  
 304 OMI/MLS ozone and Goddard Modeling Initiative (GMI) CTM simulations to quantify the



causes of the inter-annual variability (IAV) of tropospheric ozone over four sub-regions of the southern hemispheric tropospheric ozone maximum. They found that the IAV of the stratospheric ozone contribution is the most important factor driving the IAV of upper tropospheric ozone even over two selected tropical regions: the tropical south Atlantic and tropical S.E. Pacific. Emission influence on the tropospheric ozone variations at inter-annual and long-term scale in general is much weaker compared to that from STE in the middle and upper troposphere. The strong influence of emission on ozone IAV is largely confined to the subtropical South Atlantic region in September at and below ~430 hPa.

313

## 6. Time Series.

315

With about 12 years of measurements from OMI/MLS we can analyze variability from monthly to decadal timescales of the OMI/MLS residual cloud ozone and compare these changes with background ozone. In Figure 7 we show eight selected regions of interest for background ozone (top) and cloud ozone (bottom) for October 2006. For these eight selected regions we have averaged cloud ozone and background ozone each month to generate long-record time series starting October 2004.

322

Time series of the monthly background ozone and cloud ozone for the eight regions are plotted in Figures 8 and 9. In all of these eight panels the background ozone is plotted as the thick solid curve while cloud ozone is the thin curve with asterisks. Also plotted for the six landmass regions in Figures 8-9 are time series of the OMI aerosol index (dotted blue curves). In Figure 8 for northern Africa we include a line plot of the solar MgII UV index (blue squares) for comparing decadal changes in ozone in all eight panels in Figures 8-9 with the 11-year solar cycle. In the eastern Pacific region in Figure 9 the Nino 3.4 index (blue squares) is also plotted to demonstrate the dependence of cloud ozone variability from ENSO in this particular region. All background ozone and aerosol time series in Figures 8-9 were flagged missing wherever (at  $1^\circ \times 1.25^\circ$  gridding) and whenever (monthly means) corresponding measurements for cloud ozone were missing.

334



335 Figure 8 compares ozone time series for the following four regions: Central America, South  
336 America, northern Africa, and southern Africa. With the exception of the southern Africa  
337 region, the background ozone is larger than cloud ozone by ~10-20 ppbv year round. For  
338 southern Africa the cloud ozone each year in summer months exceeds background ozone by ~5-  
339 10 ppbv on average. The annual cycle for cloud ozone with southern Africa does not appear to  
340 be in phase with background ozone, reaching its annual maximum about 1-2 months earlier. The  
341 aerosol index time series in Figure 8 for southern Africa represents seasonality of biomass  
342 burning in the region and it also peaks 1-2 months prior to maximum background ozone.  
343 Sporadic thick clouds in the presence of tropospheric ozone from biomass burning via nearby  
344 regions may explain the higher ozone values and 1-2 month phase lead for cloud ozone relative  
345 to background ozone.

346

347 With Central America in Figure 8 (upper left panel) some of the month-to-month maxima and  
348 minima for cloud ozone coincide with relative maxima and minima in background ozone on  
349 intra-seasonal time scale. The Central America region including the Caribbean Sea/Gulf of  
350 Mexico and extending into the tropical north Atlantic is well documented for intra-seasonal  
351 variability in winds and cyclonic development (e.g., Park and Schubert, 1993; Maloney and  
352 Hartmann, 2000; Mo, 2000; Foltz and McPhaden, 2004, 2005). Seasonal variability in Figure 8  
353 for both background ozone and cloud ozone is most pronounced for southern Africa and weakest  
354 for northern Africa.

355

356 For decadal time scale, the background ozone in all four regions in Figure 8 is mostly invariant  
357 while cloud ozone shows small decreases toward the middle of the record followed by small  
358 increases afterward. Comparing with the MgII index in the upper right panel, this decadal  
359 variability for cloud ozone does not appear to be directly related to the 11-year cycle in solar UV  
360 which has minima centered around year 2009 and also at the end of the record.

361

362 Figure 9 shows time series for four additional regions: India/east Asia, Indonesia, eastern Pacific,  
363 and Australia. With the exception of Australia (lower right panel), the background ozone is  
364 larger than cloud ozone by ~10-20 ppbv year round. The cloud ozone and background ozone for  
365 Australia are comparable during July-November months (i.e., similar to southern Africa in



Figure 8). For Indonesia and the eastern Pacific the cloud ozone is sometimes very low to even near zero which is indicative of clean air with low concentrations of boundary-layer ozone and ozone precursors. Indonesia in Figure 9 indicates intra-seasonal variability for both cloud ozone and background ozone. In this western pacific region the main source of intra-seasonal variability of tropospheric ozone is the 1-2 month Madden-Julian Oscillation (e.g., Ziemke et al., 2015, and references therein).

Decadal changes of cloud ozone in Figure 9, with the exception of the eastern Pacific, appears again to have relative minima around the middle of the long record and no clear connection with the 11-year solar cycle in UV. Included in the panel for the eastern Pacific region is the Nino 3.4 index time series (squares along bottom) which was re-scaled for plotting with the ozone. For the eastern Pacific it is clear that there is dominant inter-annual variability related to ENSO events with associated changes in convection/SST (i.e., opposite correlation between them is indicated). For this eastern Pacific region the cloud ozone is greatest during La Nina (suppressed convection in the region) and lowest during El Nino (enhanced convection in the region).

It is difficult to discern timing of the seasonal minima and maxima of the aerosol and ozone time series in Figures 8-9. For this reason we have included Figure 10 that compares 12-month climatologies of background ozone, cloud ozone, and aerosol index time series for the six landmass regions plotted in Figures 8-9. One main conclusion from Figure 10 is that seasonal maxima of background ozone for the landmass regions of southern Africa, India/east Asia, and Australia all tend to occur about one month after maxima in aerosols. For southern Africa and India/east Asia the aerosol maximum occurs around the same month as the maximum in cloud ozone. These phase shifts suggest that biomass burning during the mostly dry season has an important impact on the seasonal cycles of tropospheric ozone including India where monsoon does not generally begin until late May or early June. It is beyond the scope of our study to explain the relative amplitude differences and phase shifts between background and cloud ozone measurements. Explaining these characteristics will require a future investigation using either a chemical transport model or a chemistry climate model with an appropriate convection scheme.

## 7. Summary.



397

398 We applied a residual technique to derive a data record (October 2004-recent) of tropospheric  
399 ozone mixing ratios inside deep convective clouds in the tropics and subtropics from OMI/MLS  
400 satellite measurements. This residual technique makes use of the cloud optical centroid pressure  
401 (OCP) obtained from the effects of rotational-Raman scattering in the OMI UV spectra. Solar  
402 UV penetrates deep into thick clouds, often by several hundred hPa. In addition, deep  
403 convective clouds have high cloud tops often near or at tropopause level. As a result the  
404 OMI/MLS cloud ozone measurements are largely indicative of ozone concentrations lying inside  
405 the clouds.

406

407 The OMI/MLS residual cloud ozone was compared with OMI/MLS near clear-sky ozone  
408 (denoted “background” ozone) indicating substantially lower concentrations (by ~10-20 ppbv)  
409 for cloud ozone year round, with the exception of southern Africa and Australia during July-  
410 November months. For both southern Africa and Australia the seasonal maxima of cloud ozone  
411 was found to exceed seasonal maxima of background ozone by about 5-10 ppbv. For both  
412 southern Africa and India/east Asia the seasonal maxima for both OMI aerosols and cloud ozone  
413 occurs about 1-2 months earlier than for background ozone. The analyses imply a cause and  
414 effect relation between boundary layer pollution and elevated ozone inside thick clouds over  
415 land-mass regions including southern Africa and India/east Asia.

416

417 While large cloud ozone concentrations ~60 ppbv or greater occur over landmass regions of  
418 India/east Asia, South America, southern Africa, and Australia, very low cloud ozone is  
419 persistent over the Indian Ocean and eastern/western Pacific Ocean with values ~10 ppbv or  
420 smaller. A low concentration of cloud ozone measured in these oceanic regions is indicative of  
421 generally pristine air with small amounts of ozone and ozone precursors in the marine boundary  
422 layer/low troposphere.

423

424 There is indication of intra-seasonal variability in cloud ozone over the eastern and western  
425 Pacific Ocean regions and also over Central America. In the western Pacific the intra-seasonal  
426 variability originates largely from the 1-2 month Madden-Julian Oscillation. In the eastern  
427 Pacific the largest variability is inter-annual and originates from ENSO and associated changes



428 in SST/convection. In the eastern Pacific the highest cloud ozone occurs during La Nina  
429 (suppressed convection over the region) with lowest cloud ozone during El Nino (enhanced  
430 convection).

431

432 Understanding changes in convection versus changes in emissions and how they relate to the  
433 variabilities in measured cloud ozone is beyond the scope of our study. A photochemical model  
434 involving deep convective clouds would be necessary to study the variability for cloud ozone  
435 from monthly to decadal time scale. Strode et al. (2017) is current work in progress that  
436 combines these OMI/MLS measurements with a chemistry-climate model to evaluate properties  
437 of cloudy versus clear-sky background ozone.

438

439 The monthly gridded cloud ozone and background ozone data can be obtained via anonymous ftp  
440 from the following:

441

```
442 > ftp jwocky.gsfc.nasa.gov  
443 > Name: anonymous  
444 > Password: (your email address)  
445 > cd pub/ccd/data_monthly  
446 > get vmr_30s_to_30n_oct04_to_apr16.sav
```

447

448

449

450 **Acknowledgments.** The authors thank the Aura MLS and OMI instrument and algorithm teams  
451 for the extensive satellite measurements used in this study. OMI is a Dutch-Finnish contribution  
452 to the Aura mission. Funding for this research was provided in part by NASA  
453 NNH14ZDA001N-DSCOV.

454

455

456

457

458





459

460

461

## 462 **References.**

463

464 Barth, M. C., P. G. Hess, and S. Madronich, Effect of marine boundary layer clouds on  
465 tropospheric chemistry as analyzed in a regional chemistry transport model, *J. Geophys. Res.*,  
466 107, (D11), 4126, 2002.

467

468 Chandra, S., J. R. Ziemke, W. Min, and W. G. Read, Effects of 1997-1998 El Nino on  
469 tropospheric ozone and water vapor, *Geophys. Res. Lett.*, 25, 3867-3870, 1998.

470

471 Fishman, J., C. E. Watson, J. C. Larsen, and J. A. Logan, Distribution of tropospheric ozone  
472 determined from satellite data, *J. Geophys. Res.*, 95(D4), 3599-3617, 1990.

473

474 Folkins, I., C. Braun, A. M. Thompson, and J. Witte, Tropical ozone as an indicator of deep  
475 convection, *J. Geophys. Res.*, 107 (D13), doi:10.1029/2001JD001178, 2002.

476

477 Foltz, G. R., and M. J. McPhaden, The 30–70 day oscillations in the tropical Atlantic, *Geophys.*  
478 *Res. Lett.*, 31, L15205, doi:10.1029/2004GL020023, 2004.

479

480 Foltz, G. R., and M. J. McPhaden, Mixed layer heat balance on intra-seasonal time scales in the  
481 northwestern tropical Atlantic Ocean, *J. Clim.*, 18(20), 4168 – 4187, 2005.

482

483 Hartmann, D. L., A. M. G. Klein Tank, M. Rusticucci, L. V. Alexander, S. Brönnimann, Y. Charabi,  
484 F. J. Dentener, E. J. Dlugokencky, D. R. Easterling, A. Kaplan, B. J. Soden, P. W. Thorne, M. Wild  
485 and P. M. Zhai,, Observations: Atmosphere and Surface. In: *Climate Change 2013: The Physical*  
486 *Science Basis. Contribution of Working Group I to the Fifth Assessment Report of the*  
487 *Intergovernmental Panel on Climate Change* [Stocker, T. F., D. Qin, G.-K. Plattner, M. Tignor, S. K.  
488 Allen, J. Boschung, A. Nauels, Y. Xia, V. Bex, and P.M. Midgley (eds.)], Cambridge University  
489 Press, Cambridge, United Kingdom and New York, NY, USA, 2014.



490

491 Huntrieser, H., et al., On the origin of pronounced O<sub>3</sub> gradients in the thunderstorm outflow  
492 region during DC3, J. Geophys. Res. Atmos., 121, 6600–6637, doi:10.1002/2015JD024279,  
493 2016.

494

495 Joiner J., and P. K. Bhartia, The determination of cloud pressures from rotational-Raman  
496 scattering in satellite backscatter ultraviolet measurements. J. Geophys. Res., 100, 23,019-  
497 23,026, 1995.

498

499 Joiner, J., A. P. Vasilkov, D. E. Flittner, J. F. Gleason, and P. K. Bhartia, Retrieval of cloud  
500 pressure and oceanic chlorophyll content using Raman scattering in GOME ultraviolet spectra, J.  
501 Geophys. Res., 109, D01109, doi:10.1029/2003JD003698, 2004.

502

503 Joiner, J., and A. P. Vasilkov, First results from the OMI rotational Raman scattering cloud  
504 pressure algorithm, IEEE Trans. Geosci. Rem. Sens., 44, 1272-1282, 2006.

505

506 Joiner, J., M. R. Schoeberl, A. P. Vasilkov, L. Oreopoulos, S. Platnick, N. J. Livesey, and P. F.  
507 Levelt (2009), Accurate satellite-derived estimates of the tropospheric ozone impact on the  
508 global radiation budget, Atmos. Chem. Phys., 9, 4447-4465, doi:10.5194/acp-9-4447-2009.

509

510 Kley, D., P. J. Crutzen, H. G.J. Smit, et. al. (1996), Observations of near-zero ozone  
511 concentrations over the convective Pacific: Effects on air chemistry, Science, 274, 230-233.

512

513 Levelt, P. F., et al., The Ozone Monitoring Instrument, IEEE Trans. Geophys. Remote Sens.,  
514 44(5), 1093-1101, 2006.

515

516 Liu, H. Y., J. H. Crawford, R. B. Pierce, et al., Radiative effect of clouds on tropospheric  
517 chemistry in a global three-dimensional chemical transport model, J. Geophys. Res., 111 (D20),  
518 D20303, 2006.

519



- 520 Liu, J. J. M. Rodriguez, S. D. Steenrod, A. R. Douglass, J. A. Logan, M. A. Olsen, K. Wargan,  
521 and J. R. Ziemke, Causes of interannual variability over the southern hemispheric tropospheric  
522 ozone maximum, *Atmos. Chem. Phys.*, 17, 3279-3299, doi:10.5194/acp-17-3279-2017, 2017.  
523
- 524 Logan, J. A., I. Megretskaya, R. Nassar, et al., Effects of the 2006 El Nino on tropospheric  
525 composition as revealed by data from the Tropospheric Emission Spectrometer (TES), *Geophys.*  
526 *Res. Lett.*, 35, L03816, 2008.  
527
- 528 Maloney, E. D., and D. L. Hartmann, Modulation of hurricane activity in the Gulf of Mexico by  
529 the Madden-Julian Oscillation, *Science*, 287, 2002 – 2004, 2000.  
530
- 531 Mo, K. C., The association between intra-seasonal oscillations and tropical storms in the Atlantic  
532 Basin, *Mon. Weather Rev.*, 128, 4097–4107, 2000.  
533
- 534 Park, C.-K., and S. D. Schubert, Remotely forced intra-seasonal oscillations over the tropical  
535 Atlantic, *J. Atmos. Sci.*, 50, 89 – 103, 1993.  
536
- 537 Sauvage, B., R. V. Martin, A. van Donkelaar, and J. R. Ziemke, Quantification of the factors  
538 controlling tropical tropospheric ozone and the South Atlantic maximum, *J. Geophys. Res.*, 112  
539 (D11) D11309, doi:10.1029/2006JD008008, 2007.  
540
- 541 Solomon, S., D. W. J. Thompson, R. W. Portmann, et al., On the distribution of and variability of  
542 ozone in the tropical upper troposphere: Implications for tropical deep convection and chemical-  
543 dynamical coupling, *Geophys. Res. Lett.*, 32, L23813, doi:10.1029/2005GL024323, 2005.  
544
- 545 Sneep, M., J. De Haan, P. Stammes, P. Wang, C. Vanbaune, J. Joiner, A. Vasilkov, and P.  
546 Levelt, Three way comparison between OMI/Aura and POLDER/PARASOL cloud pressure  
547 products, *J. Geophys. Res.*, doi:10.1029/2007JD008694, 2008.  
548
- 549 Strode, S. A., A. R. Douglass, J. R. Ziemke, M. Manyin, J. E. Nielsen, and L. D. Oman, Analysis  
550 of ozone in clear versus cloudy conditions, *J. Geophys. Res.*, in review, 2017.



551

552 Vasilkov, A. J. Joiner, R. Spurr, et al., Evaluation of the OMI cloud pressures derived from  
553 rotational Raman scattering by comparisons with other satellite data and radiative transfer  
554 simulations, *J. Geophys. Res.*, 113, D15S19, doi:10.1029/2007JD008689, 2008.

555

556 Vömel, H., and K. Diaz, Ozone sonde cell current measurements and implications for  
557 observations of near-zero ozone concentrations in the tropical upper troposphere, *Atmos. Meas.*  
558 *Tech.*, 3, 495505, doi:10.5194/amt-3-495-2010, 2010.

559

560 Zhu, B., H. Xiao, M. Huang, and Z. Li, Numerical study of cloud effects on tropospheric ozone,  
561 *Water, Air, and Soil Pollution*, 129, 199-216, 2001.

562

563 Ziemke, J. R., S. Chandra, and P. K. Bhartia, "Cloud slicing": A new technique to derive upper  
564 tropospheric ozone from satellite measurements, *J. Geophys. Res.*, 106, 9853-9867, 2001.

565

566 Ziemke, J. R., S. Chandra, B. N. Duncan, et al., Tropospheric ozone determined from Aura OMI  
567 and MLS: Evaluation of measurements and comparison with the Global Modeling Initiative's  
568 Chemical Transport Model, *J. Geophys. Res.*, 111, D19303, doi:10.1029/2006JD007089, 2006.

569

570 Ziemke, J. R., J. Joiner, S. Chandra, P. K. Bhartia, A. Vasilkov, D. P. Haffner, K. Yang, M. R.  
571 Schoeberl, L. Froidevaux, and P. F. Levelt, Ozone mixing ratios inside tropical deep convective  
572 clouds from OMI satellite measurements, *Atmos. Chem. Phys.*, 9, 573-583, 2009.

573

574 Ziemke, J. R., A. R. Douglass, L. D. Oman, S. E. Strahan, and B. N. Duncan, Tropospheric  
575 ozone variability in the tropical Pacific from ENSO to MJO and shorter timescales, *Atmos.*  
576 *Chem. Phys.*, 15, 8037-8049, doi:10.5194/acp-15-8037-2015, 2015.

577

578

579

580

581



### "Ensemble" Cloud Slicing

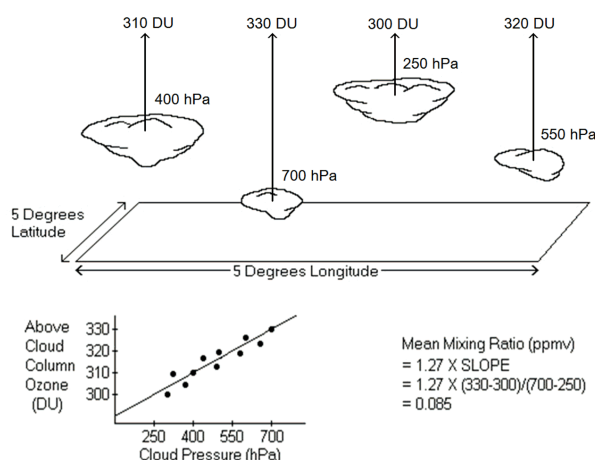


**Figure 1.** A schematic diagram illustrating the ensemble cloud slicing method involving coincident measurements of above-cloud column ozone and cloud pressure to measure mean volume mixing ratio (see text). For deep convective cumulonimbus clouds the cloud tops are near the tropopause and so the mean volume mixing ratio is primarily a measurement of average “in-cloud” ozone concentration. This figure was adapted from Ziemke et al. (2001).

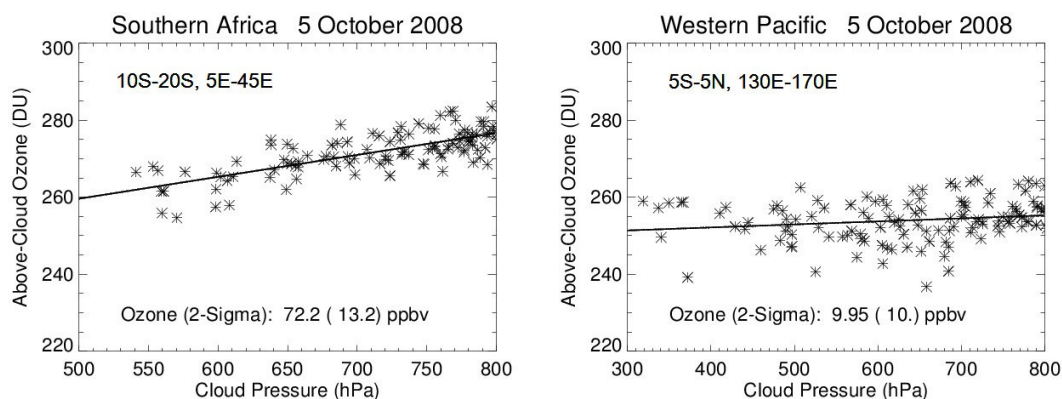
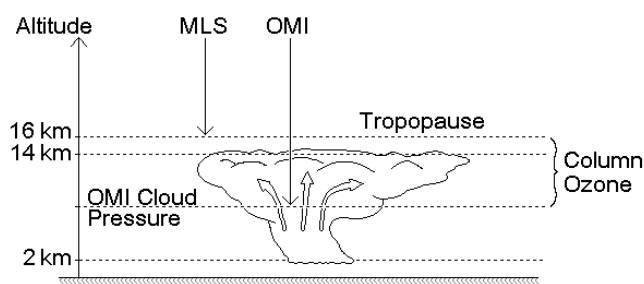


**Figure 2.** Examples of the ensemble cloud slicing technique using OMI measurements of above-cloud column ozone and cloud pressure (see text).



### Tropospheric Column Ozone Measured Over Deep Convective Clouds



610  
 611 **Figure 3.** Schematic diagram of the OMI/MLS residual cloud slicing method. This depiction  
 612 shows that deep convective clouds have OMI cloud optical centroid pressures (OCPs) lying deep  
 613 inside the clouds with cloud tops often at tropopause level or very close to the tropopause. This  
 614 figure was adapted from Ziemke et al. (2009).

615  
 616  
 617  
 618  
 619  
 620  
 621  
 622



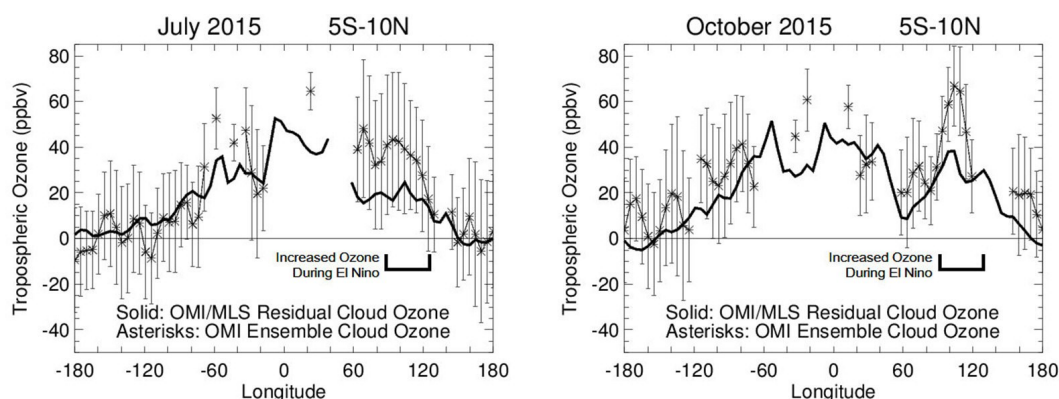


**Figure 4.** Comparisons of OMI/MLS (solid) and OMI ensemble (asterisks) cloud ozone VMR for July and October 2015 with both months coinciding with the intense 2014-2016 El Nino event. Measurements are averaged over the 5°S-10°N latitude band as a function of longitude (at 5° increments). The ensemble measurements include calculated  $\pm 2\sigma$  uncertainties. Mean VMR for the ensemble measurements are calculated for all OCP's lying between 250hPa and 550 hPa and radiative cloud fractions > 80%.

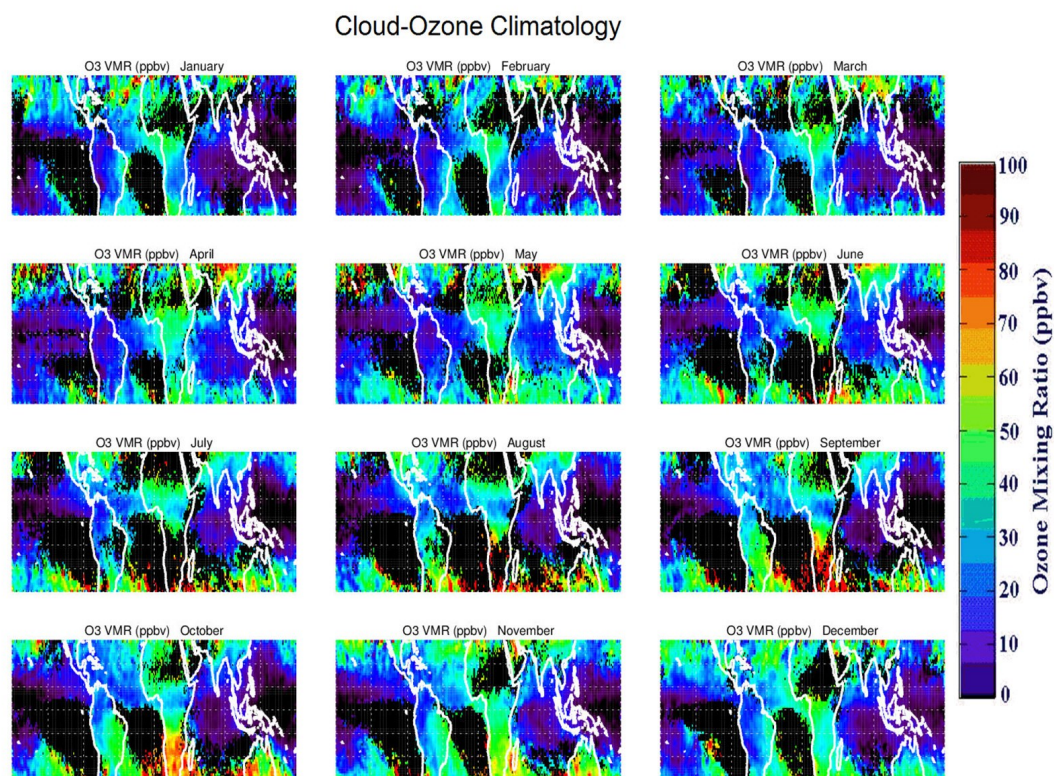
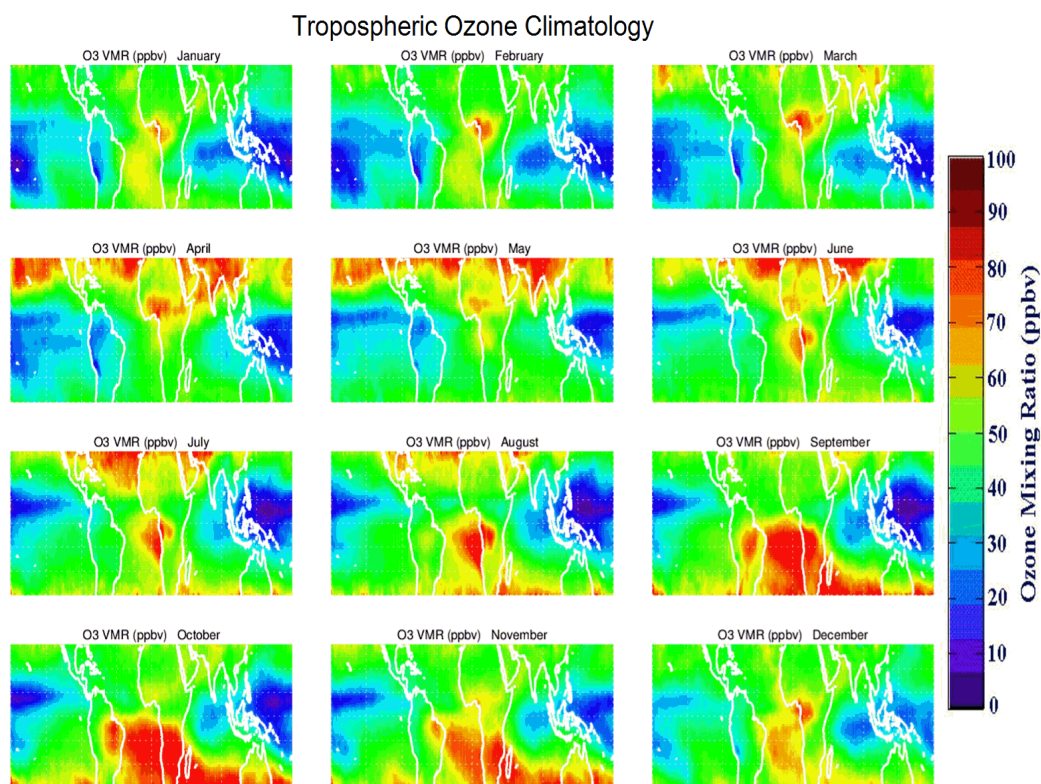
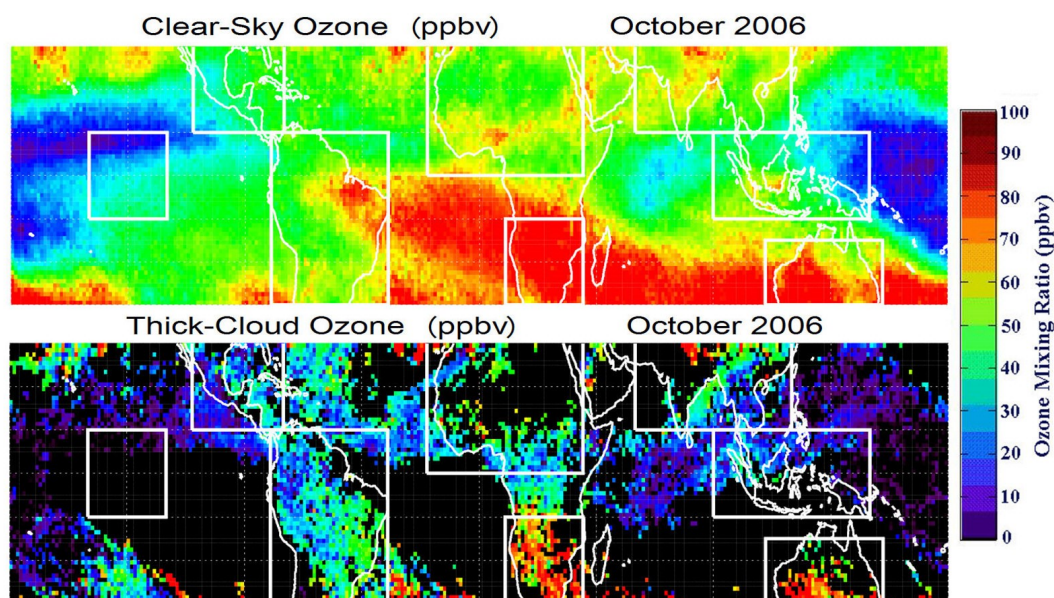


**Figure 5.** Monthly-mean climatology maps of OMI/MLS residual cloud ozone (units ppbv). Plotted is mean VMR representing average ozone concentration lying between the tropopause and OMI UV cloud pressure (OCP) as described in Section 3. The mean mixing ratio is calculated for OCPs varying between 250 hPa and 550 hPa. Black regions indicate not enough deep convective clouds present or mostly low clouds such as marine stratus clouds with OCP lying below the 550 hPa threshold.



645  
 646 **Figure 6.** Similar to Figure 5, but instead plotting monthly-mean climatology maps of  
 647 OMI/MLS VMR (units ppbv) for OMI near clear-sky scenes (i.e., radiative cloud fractions less  
 648 than 30%).  
 649



650  
 651 **Figure 7.** (Top) Background (near clear-sky) tropospheric ozone in units ppbv for October  
 652 2006. Shown as white rectangles are eight selected regions of interest where measurements are  
 653 averaged each month to generate long record time series for October 2004 – April 2016.  
 654 (Bottom) Same as top but instead for cloud ozone.

655

656



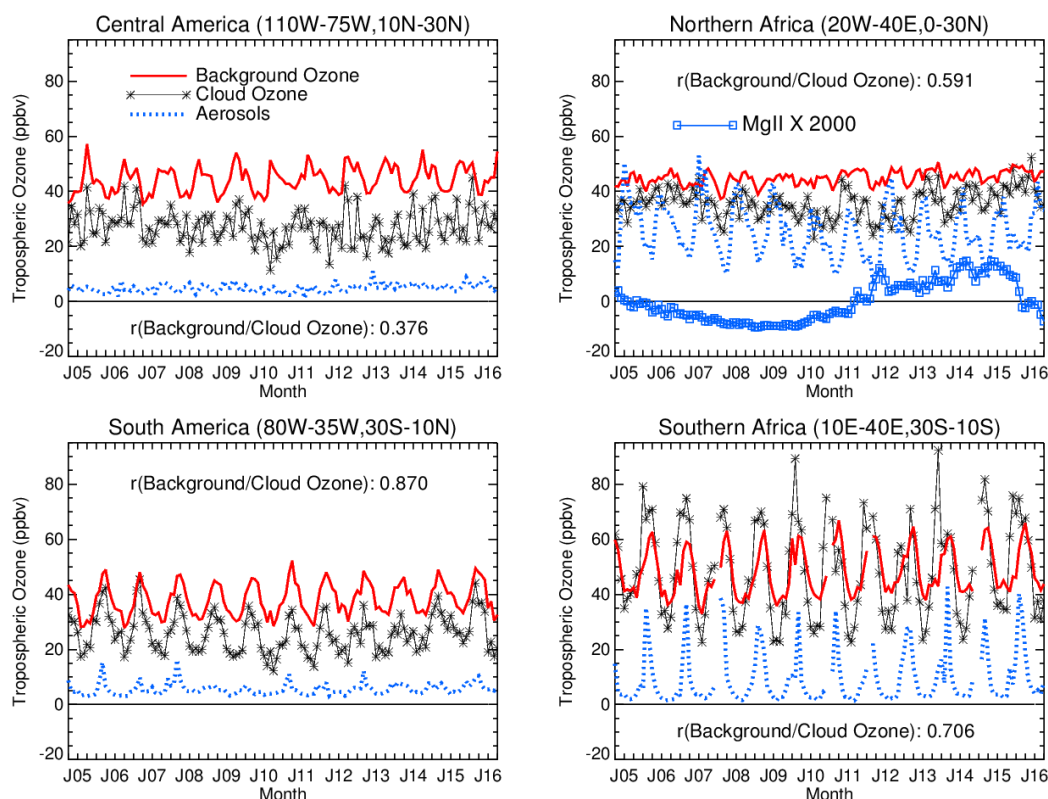
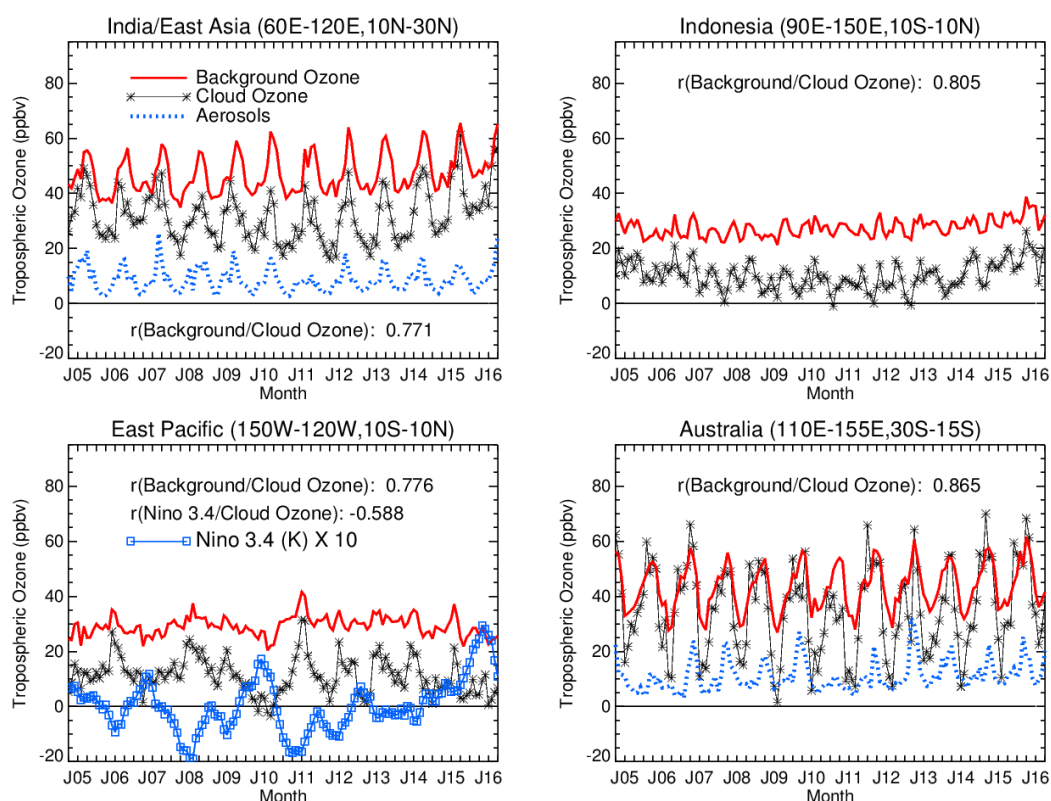


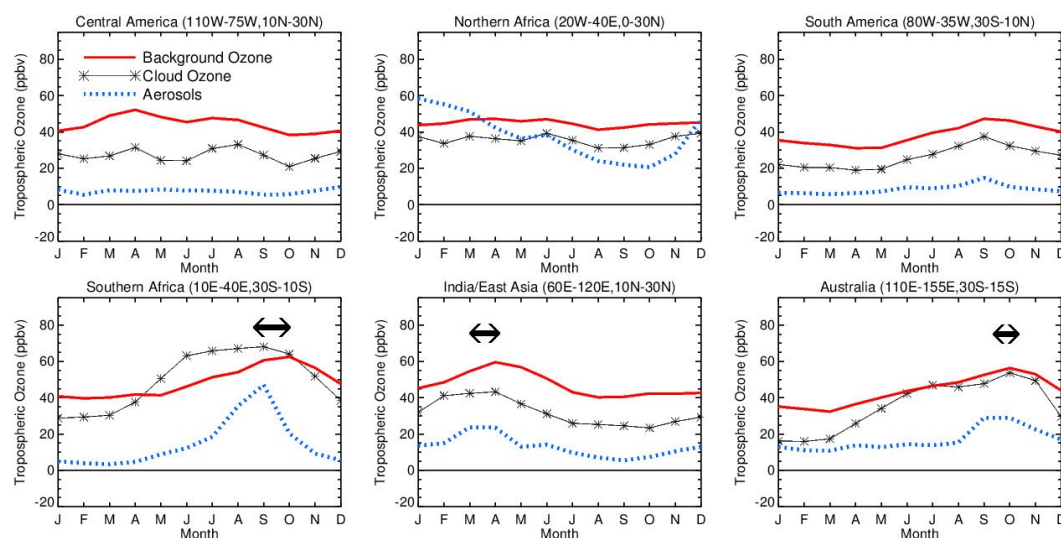
**Figure 8.** Monthly time series of background ozone (thick solid red curves) and cloud ozone (thin black curves with asterisks) for the regions of Central America, South America, northern Africa, and southern Africa in Figure 7. All ozone units are ppbv. Also shown for each of these landmass regions is the OMI monthly aerosol index time series (dotted blue curves, no units) which was re-scaled (i.e., multiplied by 60) for plotting. Included for the northern Africa region is the solar MgII index (SI units) that has been re-scaled for plotting (i.e., average removed and then multiplied by 2000).



666

667 **Figure 9.** Similar to Figure 8, but instead for the regions of India/east Asia, Indonesia, eastern  
 668 Pacific, and Australia. Aerosol index time series (dotted) for the landmass regions is again  
 669 shown. Also included for the eastern Pacific (lower left panel) is the Nino 3.4 index (blue  
 670 squares, units K) and its correlation with cloud ozone. The Nino 3.4 index was re-scaled  
 671 (multiplied by 10) for plotting with ozone time series.

672



673

674 **Figure 10.** Twelve-month climatology time series for the six continental land-mass regions  
 675 plotted in Figures 8 and 9 using the same color scheme. Shown here are background ozone  
 676 (solid red curves), cloud ozone (asterisks), and aerosol index (dotted blue curves). The OMI  
 677 aerosol index has been re-scaled (i.e., multiplied by 60) for plotting. Approximate phase shifts  
 678 between background ozone and aerosol index time series are shown with dark arrows.

679